Pneumatic-Probe Measurement Errors Caused by Fluctuating Flow Angles[‡]

John D. Coull[*]

University of Oxford, United Kingdom

Henry C.-H. Ng[**]

University of Liverpool, United Kingdom

Tony Dickens[†]

University of Cambridge, United Kingdom

José Serna[⁑]

Universidad Politécnica de Cartagena, Spain

Kenan Cengiz[††]

Leibniz University Hannover, Germany

Pneumatic probes such as Five-Hole Probes (5HP) can conveniently measure three-dimensional flow angles, plus total and static pressure. In most applications, transducers are connected using pneumatic tubes, allowing the probe head to be highly miniaturized and robust. However, such "steady" probes are often used in

---

[‡] An early version of this work was presented by Coull, J., Dickens, T., Ng, H. and Serna, J., 2020, "Five hole probe errors caused by fluctuating incidence." *XXV Symposium on Measuring Techniques in Turbomachinery, Santorini, Greece, Sept 2020*

[*] Corresponding author. Senior Research Fellow, Department of Engineering Science. john.coull@eng.ox.ac.uk

[**] Lecturer in Mechanical Engineering. Formerly at RMIT University, Australia

[†] Research Fellow. Now at Cambridge Consultants Ltd., United Kingdom

[⁑] Titular Professor

[††] Post-Doctoral Researcher

unsteady flows, where they measure a pneumatically-averaged flow field that can differ from the time-mean.

To better understand these pneumatic averaging effects, an analytical framework is constructed using a quasi-steady model. Total and static pressure coefficients have a symmetric response to both positive and negative incidence. When incidence fluctuates, there is therefore a bias in the pneumatic average. These errors are evident in a shedding wake experiment, where a 5HP over-estimates total pressure loss by up to 44% compared to a Kiel probe. These effects can be predicted by coupling an Unsteady-Reynolds-Averaged-Navier-Stokes (URANS) calculation with the quasi-steady model.

By predicting pneumatic averaging errors, the quasi-steady model can be used to obtain like-for-like validation of calculations against experimental data. Measurement data can also be corrected, provided flow angle fluctuations can be measured or estimated. This approach can be readily used to post-correct the large body of historical data likely to have been corrupted by pneumatic-averaging errors.

Nomenclature

A	sinusoidal perturbation amplitude
C	calibration coefficient
C_D	drag coefficient
C_p, C_{ps}	pressure coefficients, eq (33), (38)
d	probe diameter
D	dynamic pressure coefficient $= f(t)$

E	error
f	frequency
f_r	reduced frequency
F_D	drag force
h	span
H	channel height
P	pressure
u, v, w	fluctuating velocity components
V	time-mean streamwise velocity
St	Strouhal number
t	time
W	width
x	axial direction
y	transverse direction
α	flow angle
λ	disturbance wavelength
ρ	density
ϕ	phase angle

Sub-scripts

0	total

1	inlet
2	traverse plane
ave	average
$comp$	compound
cor	corrected
dyn	dynamic pressure
fs	freestream
pit	pitch
RMS	root-mean-squared fluctuation
s	static

Over-bars

$\bar{}$	time-averaged
$\hat{}$	pneumatically-averaged

I. Introduction

Many aerodynamic flows are highly three-dimensional by nature. The velocity components may be obtained from laser techniques (e.g. stereoscopic Particle Imaging Velocimetry) or hot-wire anemometry. However, such methods do not measure total pressure, which is often required to characterize performance, especially for internal flows. Velocity and pressure measurements are most readily obtained using calibrated multi-hole probes, such as the five-hole-probe (5HP) shown in Figure 1(a). This paper considers “steady” probes, where pneumatic tubing connects the probe head to the transducer, which only records averaged pressures. Steady 5HPs have many advantages. They are relatively simple to construct, low-cost and easy to operate. They can be made at small scale

(~1mm diameter) to minimise spatial errors, e.g. Grimshaw and Taylor [1], and enable measurement access, e.g. for intra-row traverses in multi-stage turbomachines. Furthermore, these probes can be made sufficiently robust to operate in harsh environments. With these advantages, steady muti-hole probes are widely used in a range of applications.

"Steady" pneumatic probes are often used when there is significant unsteadiness in the flow. A key example is the measurement of turbomachinery performance, which often relies on stationary-frame 5HP traverses downstream of rotating blade rows, e.g. Bauinger et al. [2], Evans and Longley [3] and Prahst et al. [4]. Other set-ups with significant unsteadiness include measurements in shedding wakes., e.g. Melzer and Pullan [5] used a un-Kieled pitot to assess shedding trailing edge loss. In such unsteady flows, it has been generally recognised that the pneumatic-averaged flow indicated by these steady probes may differ from the true time-average. However, these effects are poorly understood and are usually ignored.

This work is thus motivated by the need to address the deficiency in our understanding of pneumatic-averaging. By focusing on long-wavelength unsteadiness, we develop a simple, rigorous approach to explain and quantify the resultant errors. We focus on 5HPs, but the analysis is equally applicable to other multi-hole pneumatic probes, and un-Kieled pitots.

A. Previous Studies of Pneumatic-Averaging

Most previous studies of pneumatic averaging considered small-scale turbulence. For a pitot tube, Goldstein [6] argued that the turbulent kinetic energy will be reversibly recovered if the eddies are small compared to the probe. Assuming incompressible flow, a pitot pointing into the flow will therefore indicate a total pressure $\hat{P}_0$:

$$\hat{P}_0 \approx \overline{P} + \frac{\rho}{2}\overline{V}^2 + \frac{\rho}{2}\left(\overline{u^2} + \overline{v^2} + \overline{w^2}\right) = \overline{P}_0 \qquad (1)$$

where $\bar{P}$ is the time-averaged pressure, $\bar{V}$ is the mean velocity and u, v, w are the velocity fluctuation components. By these assumptions the probe will indicate the true time-mean total pressure, $\bar{P}_0$.

In practice the Goldstein approximation is not always applicable. Bailey et al. [7] compared hot-wire and pitot measurements in boundary layers, and found that only the streamwise fluctuations contributed to the indicated total pressure:

$$\hat{P}_0 \approx \bar{P} + \frac{\rho}{2}\bar{U}^2 + \frac{\rho}{2}\overline{u^2} = \bar{P}_0 - \frac{\rho}{2}\left(\overline{v^2} + \overline{w^2}\right) \quad (2)$$

Thus the pitot indicates a total pressure below the true time-mean. A similar, but greater, effect is observed in our current analysis of 5HPs.

Few authors have examined these effects for multi-hole probes. Building on the work of Bradshaw and Goodman [8], Christiansen and Bradshaw [9] examined yaw meters at high and low turbulence and found high static pressure errors when instantaneous yaw angles were large. This work is again consistent with the current findings.

B. Quasi-Steady Pneumatic-Averaging

Rather than focus on small-scale turbulence, we here focus on large-scale flow fluctuations, which affect the pressure field around the entire probe head and can thus cause large errors. The scale of the fluctuations can be characterised using the reduced frequency f_r, which is a ratio of characteristic lengths:

$$f_r = \frac{f\,d}{V} = \frac{d}{\lambda} \quad (3)$$

where f is the frequency of the fluctuation, V is the flow velocity, d is the probe diameter and λ is the fluctuation wavelength. A reduced frequency below ~0.3 typically indicates quasi-steady behaviour. At higher reduced frequencies the flow becomes fundamentally unsteady and the probe response will depart from quasi-steady behaviour. Nonetheless the general trends are likely to be similar.

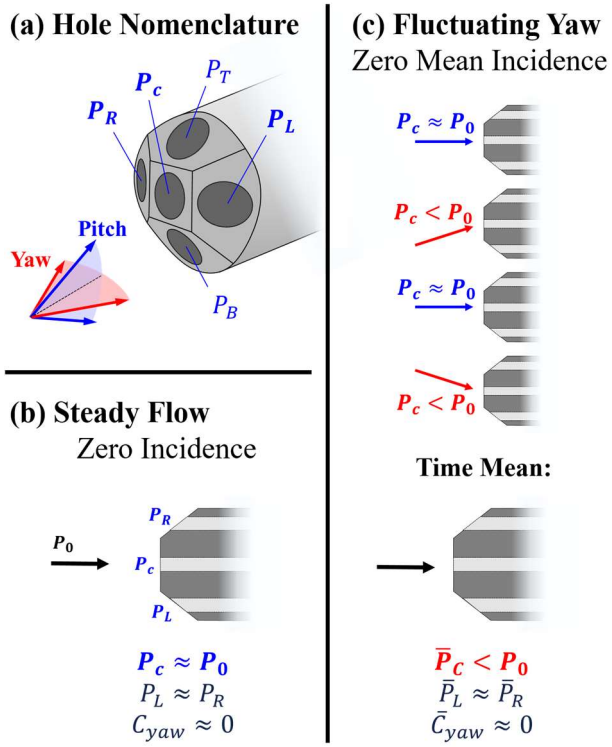

Figure 1: Five-Hole-Probe nomenclature and response in steady and fluctuating flow.

Figure 1(b) and (c) respectively illustrate the response of a 5HP to steady flow and with fluctuating yaw angle. The mean incidence is zero. In steady flow (Figure 1(b)), the central hole operates as a pitot and measures a pressure close to the flow total pressure, $P_C \approx P_0$. For fluctuating yaw (Figure 1(c)), the flow is at times aligned with the probe, $P_C \approx P_0$, but at other instances the incidence causes the central hole to measure a lower pressure, $P_C < P_0$. Thus, on average, the central hole will measure a total pressure below the true time-mean, i.e. $\bar{P}_C < \bar{P}_0$. This effect can also be inferred from Bailey's result for turbulent fluctuations, equation (2), and applies equally to simple pitots and other multi-hole probes.

The reduction in central-hole pressure ($\bar{P}_C < \bar{P}_0$) is deeply problematic for steady probes because they cannot distinguish between steady and fluctuating flow. The fluctuating flow condition is therefore interpreted simply as having lower total pressure. This effect is evident in the current experiments and in the data of Bauinger et al. [2], where a 5HP downstream of a turbine rotor indicated lower total pressure than Kiel-shrouded pitots, which are largely insensitive to angle.

C. Paper Aims and Outline

The key aims of the paper are (1) to explain how pneumatic-averaging errors arise in unsteady flow and (2) to demonstrate how to predict and correct these errors.

First, a theoretical framework is laid out: §II details the quasi-steady probe response model, and §III discusses the response of two different designs of 5HP to sinusoidal flow fluctuations. An experiment to examine unsteady flow errors and a complementary CFD calculation are described in §IV and §V respectively. §VI presents the measurements, demonstrates how these errors should be accounted for in CFD validation, and explores means to correct the experimental data. Finally, §VII considers the general implications of the findings.

II. 5HP Pneumatic-Averaging Model

A. Steady Flow Calibration Coefficients

Non-dimensional pressure coefficients obtained from the steady calibration map are indicated by the symbol C. For individual holes these are given by (Dominy and Hodson [10]):

$$C_X = \frac{P_X - P_0}{P_0 - P_s} \tag{4}$$

where P_0 is the flow total pressure, P_s is the static pressure and P_X is the pressure of the hole in question. The subscript X indicates the index of the hole: centre C, left L, right R, top T, bottom B, Figure 1(a). The average side-hole pressure coefficient C_{ave} is expressed as:

$$C_{ave} = \frac{P_{ave} - P_0}{P_0 - P_s} = \frac{(C_L + C_R + C_T + C_B)}{4} \tag{5}$$

Using these coefficients, the usual choice of yaw and pitch angle coefficients are:

$$C_{yaw} = \frac{P_L - P_R}{P_C - P_{ave}} = \frac{C_L - C_R}{C_C - C_{ave}} \tag{6}$$

$$C_{pit} = \frac{P_T - P_B}{P_C - P_{ave}} = \frac{C_T - C_B}{C_C - C_{ave}} \tag{7}$$

The total and dynamic pressure coefficients are typically taken as:

$$C_{P0} = \frac{P_0 - P_C}{P_C - P_{ave}} = \frac{-C_C}{C_C - C_{ave}} \tag{8}$$

$$C_{dyn} = \frac{P_0 - P_S}{P_C - P_{ave}} = \frac{1}{C_C - C_{ave}} \tag{9}$$

Together these coefficients can also define a static pressure coefficient, here defined as:

$$C_{PS} = \frac{P_C - P_S}{P_C - P_{ave}} = C_{dyn} - C_{P0} = \frac{C_C + 1}{C_C - C_{ave}} \tag{10}$$

Though rarely used, it is useful for the current analysis to separate static pressure in this manner.

B. Probes and Calibration Ranges

For simplicity the calibration is assumed to be independent of Reynolds and Mach number, so that $C(t) = f\big(\alpha_{yaw}(t), \alpha_{pit}(t)\big)$. The methods can be readily extended to include these effects, which will be small for well-designed probes operating below transonic Mach numbers (<0.7).

This paper uses calibration maps from two different 5HP probes, designated as:

1) ***Grimshaw 60° Probe*:** This pyramid probe has side faces set at 60° from the probe axis and a diameter of 1.5mm. The calibration covers ±60° in yaw and ±20° in pitch, Grimshaw [11].

2) ***Ng 45° Probe*:** This conical probe has faces at 45° from the probe axis and 2.2mm diameter. The calibration covers ±26° in yaw and pitch. This probe was previously used by Ng and Coull [12].

As will be seen, the two probes exhibit similar total pressure errors but different static pressure errors.

C. Sinusoidal Fluctuations

For the analysis in §III, fluctuating flow is specified by defining sinusoids of arbitrary frequency. Flow angles are given by:

$$\alpha_{yaw}(t) = \bar{\alpha}_{yaw} + A_{yaw}\, sin(t) \tag{11}$$

$$\alpha_{pit}(t) = \bar{\alpha}_{pit} + A_{pit}\, sin\big(t + \phi_{pit}\big) \tag{12}$$

where ϕ_{pit} controls the relative phase. Fluctuating pressures can be specified relative to the *true time-mean* total ($\bar{P}_0$) and static pressure ($\bar{P}_s$) of the flow:

$$D_{P0}(t) = \frac{P_0(t) - \bar{P}_0}{\bar{P}_0 - \bar{P}_s} = A_{P0}\, sin(t + \phi_{P0}) \tag{13}$$

$$D_{Ps}(t) = \frac{P_s(t) - \bar{P}_s}{\bar{P}_0 - \bar{P}_s} = A_{Ps}\, sin(t + \phi_{Ps}) \tag{14}$$

The symbol D denotes a dynamic pressure normalized by the true time-mean dynamic pressure.

D. Quasi-Steady Probe Response

As shown in Figure 2, the instantaneous response of each hole is estimated by interpolating from the calibration data. From equation (4):

$$P_X(t) = P_0(t) + (P_0(t) - P_s(t))C_X(t) \tag{15}$$

where $C_X(t) = f\big(\alpha_{yaw}(t), \alpha_{pit}(t)\big)$ interpolates the hole calibration coefficient for the instantaneous angles. Normalized by the time-mean flow, the dynamic pressure coefficients $D_X(t)$ are thus:

$$D_X = \frac{P_X - \bar{P}_0}{\bar{P}_0 - \bar{P}_s} = D_{P0} + C_X(D_{P0} - D_{Ps} + 1) \tag{16}$$

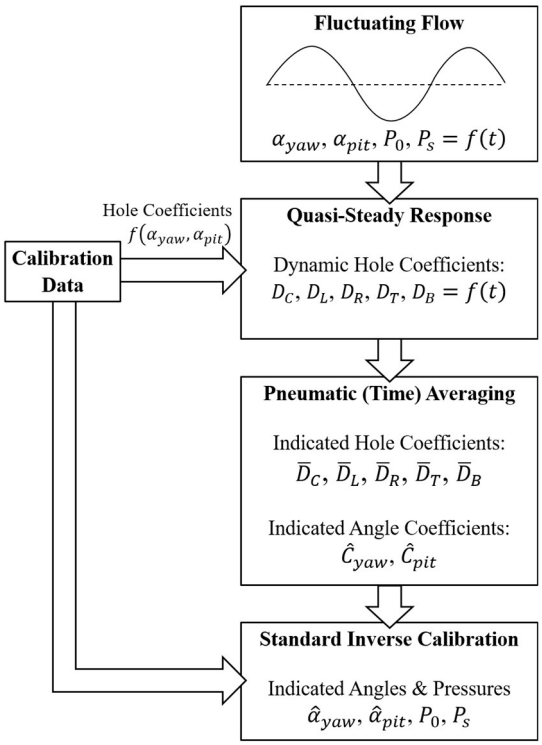

Figure 2: Quasi-Steady model.

E. Pneumatically-Averaged Response

A precise model of pneumatic averaging would need to consider the dynamics of the pressure tubes, which can affect the average readings. However, such effects are likely to be small, and thus pneumatic averaging is simply modelled by time-averaging each hole pressure, giving the following pitch and yaw coefficients:

$$\hat{C}_{yaw} = \frac{\overline{D}_L - \overline{D}_R}{\overline{D}_C - \overline{D}_{ave}} \tag{17}$$

$$\hat{C}_{pit} = \frac{\overline{D}_T - \overline{D}_B}{\overline{D}_C - \overline{D}_{ave}} \tag{18}$$

These *probe-indicated* values are denoted using over-hats, and may differ from the true time-average of the instantaneous coefficients, $\bar{C}_{yaw}$ and $\bar{C}_{pit}$.

Indicated angles are calculated by interpolating from the calibration map in typical fashion:

$$\hat{\alpha}_{yaw}, \hat{\alpha}_{pit} = f\left(\hat{C}_{yaw}, \hat{C}_{pit}\right) \tag{19}$$

The errors from the true time mean flow angles are:

$$E_{yaw} = \hat{\alpha}_{yaw} - \bar{\alpha}_{yaw} \tag{20}$$

$$E_{pit} = \hat{\alpha}_{pit} - \bar{\alpha}_{pit} \tag{21}$$

The indicated total, static and dynamic pressure coefficients are interpolated from the calibration using the indicated angles:

$$\hat{C}_{P0}, \hat{C}_{Ps}, \hat{C}_{dyn} = f\left(\hat{\alpha}_{yaw}, \hat{\alpha}_{pit}\right) \tag{22}$$

Again, these values will generally differ from the true time averages. Non-dimensional errors in the indicated total, dynamic and static pressure, are then defined relative to the true time-average flow:

$$E_{P0} = \frac{\hat{P}_0 - \bar{P}_0}{\bar{P}_0 - \bar{P}_s} = \overline{D}_C + \hat{C}_{P0}(\overline{D}_C - \overline{D}_{ave}) \tag{23}$$

$$E_{Ps} = \frac{\hat{P}_s - \bar{P}_s}{\bar{P}_0 - \bar{P}_s} = 1 + \overline{D}_C - \hat{C}_{Ps}(\overline{D}_C - \overline{D}_{ave}) \tag{24}$$

$$E_{dyn} = \frac{\hat{P}_0 - \hat{P}_s}{\bar{P}_0 - \bar{P}_s} - 1 = \hat{C}_{dyn}(\overline{D}_C - \overline{D}_{ave}) - 1 \tag{25}$$

Each error is positive when the quantity is over-estimated by the probe and vice-versa. For steady flow all errors are zero by definition.

III. Sinusoidal Flow Fluctuations

We now examine the response of the quasi-steady model to sinusoidal fluctuations, the most important of which are angle fluctuations.

A. Angle Fluctuations in One Component

For the Grimshaw probe, Figure 3 shows the response to a sinusoidal fluctuation of ±25° in yaw angle, for zero mean incidence. The instantaneous points simply follow the calibration line for $\alpha_{pit} = 0$. Because the calibration is approximately *anti-symmetric*, positive and negative incidence effects tend to cancel each other. Thus the pneumatic average Yaw Coefficient $\hat{C}_{yaw}$ is close to zero, and the probe indicates a yaw angle $\hat{\alpha}_{yaw} \approx 0°$.

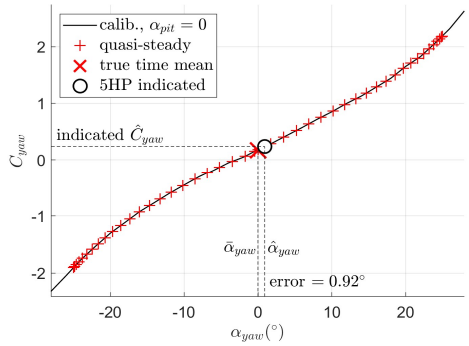

Figure 3: Yaw Angle response to ±25° fluctuating Yaw, 60° Grimshaw Probe.

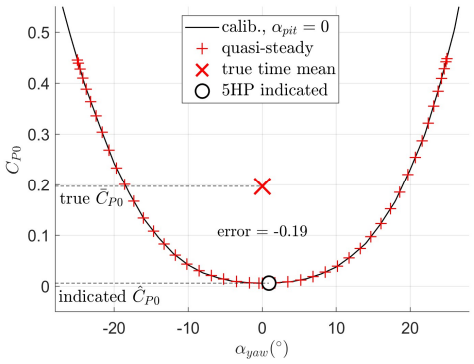

Figure 4: Total Pressure response to ±25° fluctuating Yaw, 60° Grimshaw Probe.

Figure 4 shows the total pressure response for the same fluctuation. In contrast to yaw angle, C_{P0} vs. α_{yaw} is *symmetric*. Both positive and negative yaw cause the central hole pressure to drop (higher C_{P0}); this is the process illustrated schematically in Figure 1(c). Due to this effect, the true time-average total pressure coefficient (equation (8)) is $\bar{C}_{P0} \approx 0.2$. This value is the correction that *should* be applied to the central hole pressure to give the correct flow total pressure, i.e.

$$\bar{P}_0 = \bar{P}_c + (\bar{P}_c - \bar{P}_{ave})\bar{C}_{P0} \tag{26}$$

In the absence of knowledge of fluctuations, the 5HP operator must use the indicated flow angles ($\hat{\alpha}_{yaw} \approx 0$, $\hat{\alpha}_{pit} \approx 0$) to interpolate for C_{P0} from the steady calibration data. This gives an indicated total pressure coefficient $\hat{C}_{P0} = 0.01$, which suggests that the flow total pressure should be very close to the central hole pressure. Without the correct factor ($\bar{C}_{P0} \approx 0.2$), the probe thus indicates a lower total pressure than the true value:

$$\hat{P}_0 = \bar{P}_c + (\bar{P}_c - \bar{P}_{ave})\hat{C}_{P0} \approx \bar{P}_0 - 0.19(\bar{P}_c - \bar{P}_{ave}) \tag{27}$$

The calibration map for static pressure also has a generally symmetric response to angle, but it is more sensitive to the probe design and manufacture. Figure 5 shows the static pressure response for the Grimshaw probe. Because of its high face angle (60°), the static pressure coefficient is relatively insensitive to angles over this range. Thus the underestimation of P_s in Figure 5 is only around $0.04(P_C - P_{ave})$. Figure 6 shows the response of the Ng probe, which has face angles of 45° and is more sensitive to angle. As shown, this probe underestimates static pressure by $0.37(P_C - P_{ave})$.

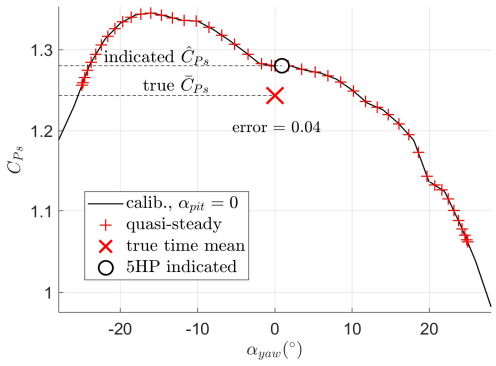

Figure 5: Static Pressure response to ±25° fluctuating Yaw, 60° Grimshaw Probe.

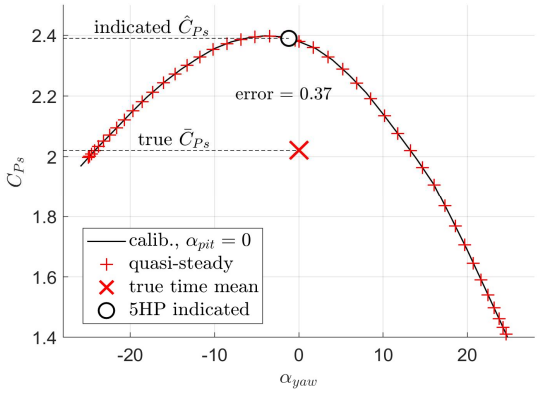

Figure 6: Static Pressure response to ±25° fluctuating Yaw, 45° Ng Probe.

B. Angle Fluctuations in Two Components

We now consider simultaneous fluctuations in both angle components. Figure 7 shows total pressure errors for a range of A_{yaw}, A_{pit} and phase ϕ_{pit} for the two probes, plotted against the root-mean-square (RMS) of the fluctuating compound angle (i.e. the standard deviation):

$$\alpha_{comp-RMS} = \sqrt{\left(\alpha_{yaw-RMS}\right)^2 + \left(\alpha_{pit-RMS}\right)^2} \tag{28}$$

The effect of probe design and phase is minimal, and the errors collapse to the following correlation:

$$E_{P0} \approx -1.6 \times 10^{-4} \left(\alpha_{comp-RMS}\right)^{2.3} \tag{29}$$

The collapse for both probes reflects the pitot-like configuration of the 5HP central hole and the similarity in pitch and yaw response. Similar errors would be expected for un-Kieled pitot measurements. Figure 7(a) includes the Bailey et al. [7] correction from equation (2), applied to the central hole. The Bailey equation is accurate for small incidence ($\alpha_{comp-RMS} < 15°$) but underestimates errors for larger fluctuations.

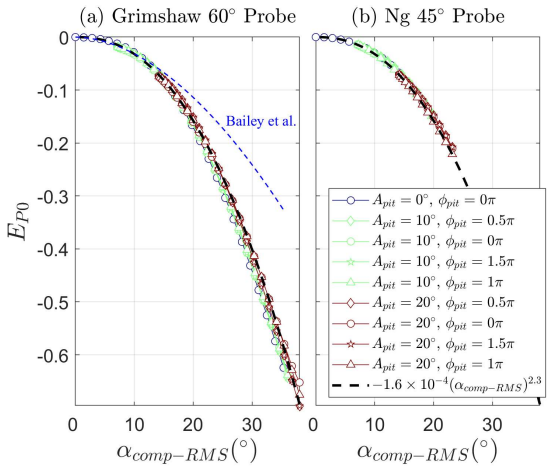

Figure 7: Total Pressure Errors for fluctuating yaw and pitch.

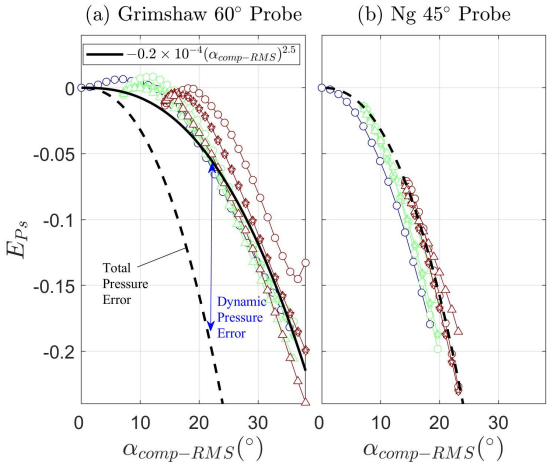

Figure 8: Static Pressure Errors for fluctuating yaw and pitch, legend in Figure 7.

The static pressure errors are presented in Figure 8; note the smaller scale compared to Figure 7. As observed above the two probes respond differently, but again the errors approximately collapse to $E_{PS} \approx f(\alpha_{comp-RMS})$. The scatter is greater than for total pressure, reflecting the poorer conditioning of the static pressure measurement, [10]. The static pressure coefficient is also less directionally symmetric than the total pressure coefficient (Figure 5, Figure 6).

The static errors for 45° Ng probe (Figure 8(b)) are approximately equal to the total errors:

$$E_{PS} \approx E_{P0} \approx -1.6 \times 10^{-4} \left(\alpha_{comp-RMS}\right)^{2.3} \tag{30}$$

As a result of these similar errors, the Ng probe has generally low dynamic pressure error.

With its sharper face angles, the 60° Grimshaw probe (Figure 8(a)) has smaller static errors which can be approximated by:

$$E_{Ps} \approx -0.2 \times 10^{-4} \left(\alpha_{comp-RMS}\right)^{2.5} \tag{31}$$

As indicated in Figure 8, this probe therefore suffers from relatively large dynamic pressure errors.

These static error correlations should provide useful initial estimates for similar probes. For greater accuracy, the quasi-steady model in §II can be readily applied to any given calibration map and flow perturbation.

C. Other Factors Affecting Errors

The flow angle effects shown above are the dominant source of pneumatic-averaging errors. Nonetheless it is worth noting other factors that can influence the errors:

- Reducing the time-averaged incidence, as in "nulled" 5HP operation, tends to slightly reduce errors but the benefits are unlikely to be significant.
- The addition of pressure fluctuations to the angle fluctuations can increase or decrease error slightly, depending on the phase. These effects are driven by the covariance of angle and pressure, which adds further biasing to the pneumatic averaging. The quasi-steady model can be used to analyse these covariance effects, but there were found to be unimportant in the current experiment.

D. Summary

The calibration maps for total and static pressure coefficient are approximately symmetric. The probe therefore effectively responds to the magnitude of a fluctuation in flow angle, $|\alpha'|$. When probe incidence fluctuates, pneumatic averaging therefore causes a bias which cannot be accounted for by the steady calibration. Having demonstrated how these pneumatic-averaging errors arise, we will now examine them in practice in a canonical bluff body flow.

IV. Experimental Set-Up

The case study is a D-shaped body in an enclosed channel, as shown in Figure 13. Air is driven through the test section by an open-loop wind tunnel. The body has a semi-circular leading edge, a width W of 80mm, chord 187.5mm and span of 375mm. The body is mounted at zero incidence in the middle of a long channel of height (H) of 650mm, giving a blockage factor of 12%. The Reynolds number was 98,500 based on the body width W and upstream velocity V_1. The flow was incompressible (Mach < 0.15), and the inlet turbulence level was 0.5%.

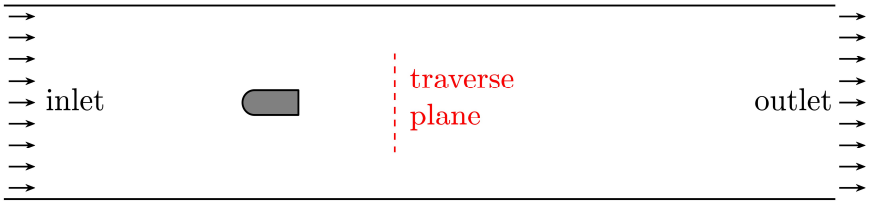

Figure 9: D-Shaped bluff body experiment.

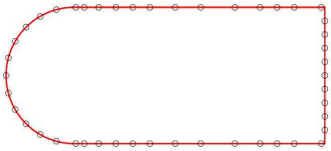

Figure 10: Surface Static Tapping Locations.

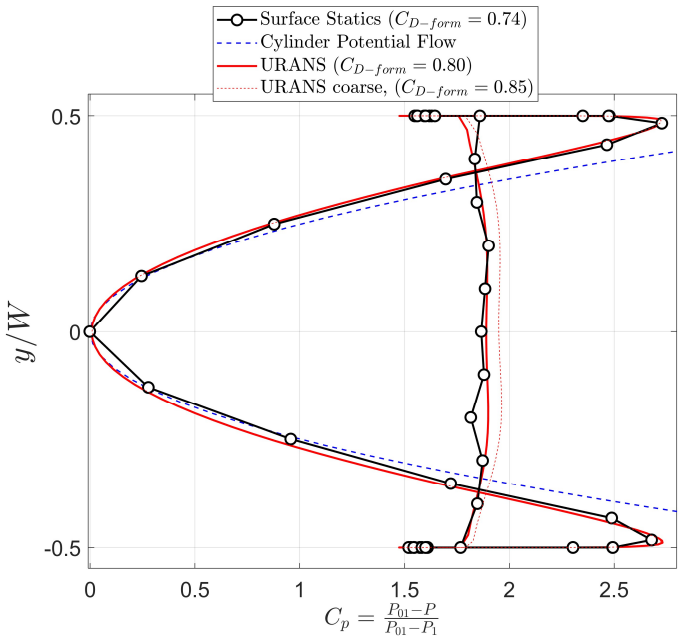

Figure 11: Surface Static Pressure Coefficient.

All pressure measurements were obtained using a Scanivalve DSA 3217 with a 10" H_20 range. The inlet total pressure P_{01} was measured using wall mounted pitots in the upstream wind tunnel, prior to a ~4:1 flow contraction into the constant-area test section. Inlet static pressure P_1 was measured on the wall centreline 600mm ($7.5W$) upstream of the leading edge.

A. Wake Traverses and Probe Reduced Frequency

Wake traverses were obtained with the Ng 5HP probe described in section B. This probe has a conical head with 45° face angles and a diameter of 2.2mm ($0.035W$). The probe was calibrated in a separate facility for ±26° yaw and pitch, at a similar velocity as in the experiments. Using an automated stepper-motor controller, traverses were obtained along the midspan plane at a streamwise distance of 323mm ($\approx 4W$) behind the trailing edge, covering a vertical height of 0.34m (= $4.25W$) which fully captured the wake.

The reduced frequency of the 5HP probe (equation (3)) can be related to the flow Strouhal number ($St = fW/V_1$):

$$f_r = \frac{f\,d}{V} = \frac{d}{\lambda} = St\frac{V_1}{V}\frac{d}{W} \tag{32}$$

where V is the local velocity at the probe head. The velocity ratio V_1/V varies between about 0.9 and 1.4 through the wake traverse, and the probe diameter is small relative to the body width, $d/W = 0.035$. For the primary shedding frequency ($St \approx 0.2$), the reduced frequency is $f_r \approx 0.01$ and the probe will respond quasi-steadily.

The 5HP measurements were complemented by traversing a Kiel probe (Kiel-shrouded-pitot) of 4mm outer diameter at the same location. This Kiel probe is insensitive to flow angle over a range of at least ±30° and therefore does not suffer from significant biasing errors as flow angles fluctuate. An array of 11 static tappings were also situated on the side wall at the traverse plane, clustered towards the centreline and covering the full traverse height. Area traverses with the 5HP and Kiel probe showed that the flow is approximately two-dimensional over the central 60-70% of span.

B. Surface Static Pressure and Form Drag

Forty-six surface static tappings were distributed around the D-shaped body as shown in Figure 10. The measured static pressure coefficients are shown in Figure 11:

$$C_p = \frac{P_{01} - P}{P_{01} - P_1} \tag{33}$$

As can be seen, the front face pressures largely follow the potential flow theory distribution for a cylinder, while the trailing face has near-constant pressure. The form drag coefficient can be calculated by integration:

$$C_{D-form} = \oint \frac{C_p dy}{W} \tag{34}$$

For this flow the form drag will dominate over viscous shear and one expects $C_D \approx C_{D-fo}$. Numerical integration using cubic interpolation between measurement points gives a form drag coefficient of 0.74.

C. Drag Coefficient from Wake Traverses

The drag coefficient is also calculated from the wake traverse after the method of Jones [13]. A virtual downstream plane is considered which has the same static pressure as the inlet, P_1. The drag coefficient is then given by:

$$C_D = \frac{F_D}{\frac{1}{2}\rho V_1^2 W} = 2\frac{\theta'}{W} \tag{35}$$

The wake momentum thickness θ' at the virtual plane is calculated by assuming two-dimensional flow from the traverse plane, applying continuity and assuming isentropic flow:

$$\theta' = \int \sqrt{\frac{P_{02} - P_2}{P_{01} - P_1}} \left(1 - \sqrt{\frac{P_{02} - P_1}{P_{01} - P_1}}\right) dy \tag{36}$$

The value of C_D is sensitive to the assumptions made, but alternative calculation methods show the same trends observed in the current analysis.

V. Computational Methods

To complement the measurement data, a URANS calculation of the experiment is performed. As well as allowing comparison of predictions and experiments, this calculation provides an estimate of unsteady flow angles and demonstrates the need to mimic the pneumatic-averaging errors when validating CFD.

A. URANS Set-Up

The URANS calculation was performed with Fluent v18.2 using a pressure-based incompressible solver, with second order accuracy in space and time. Full details of the governing equations are given in reference [14]. A midspan cross-section of the domain is shown in Figure 12. The full span ($4.69W$) was simulated over an axial distance of 6.5 chords ($\sim 15.2W$). The figure also shows the mesh, which is a multi-block structured mesh with 5.8 million cells. Wall functions are used to resolve the boundary layers: with the exception of the trailing edge, a constant first cell width of $0.009W$ was used on all viscous surfaces, giving a first cell y^+ between 40 and 80 over the body surface and sidewalls. Mesh sensitivity is considered in the following sub-section.

Boundary conditions are applied to mimic the experiment. The average static pressure at domain exit was set to be atmospheric. At the inlet, uniform values of total pressure (225 Pa gauge), turbulence intensity (1%) and turbulent viscosity ratio (10) are specified. Constant density (1.225 kg/m^3) and dynamic viscosity (1.7894×10^{-5} kg/ms) are assumed. The side-walls are treated as viscous walls, while the top and bottom walls of the domain were set to be inviscid walls: a separate calculation showed that this approximation had no significant impact on the results. In order to duplicate the experimental post-processing, the inlet reference pressure P_1 was taken as the area- and time-average at the inlet at midspan. Around 100 timesteps were used for each fundamental shedding cycle, and data were collected for approximately 40 cycles after initial transients.

Turbulence is modelled using the Scale-Adaptive-Simulation model of Menter and Egorov [15], which has been developed specifically to help capture the multiple scales of vortex interaction and

shedding flows. The presence of multiple vortex scales is evident in Figure 13, which shows a snapshot of turbulent kinetic energy from the URANS calculation. Figure 14 shows time traces of angles at the centreline of the traverse plane for around 12 shedding cycles. Yaw oscillations (within the plane of Figure 13) of over ±35° are observed, with smaller variation in pitch.

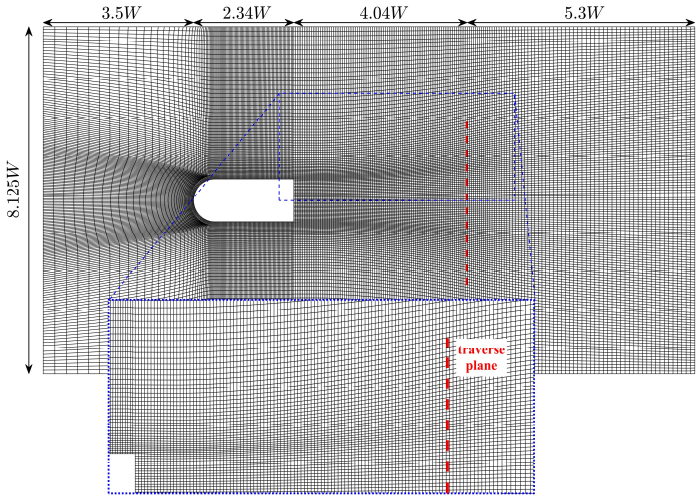

Figure 12: URANS domain and fine grid, midspan plane.

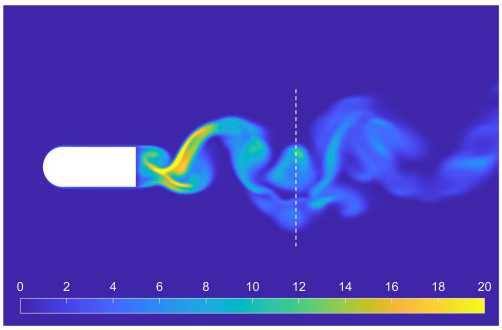

Figure 13: Instantaneous Turbulent Kinetic Energy (m^2/s^2) in the midspan plane, URANS (fine mesh). Dashed line indicates traverse plane.

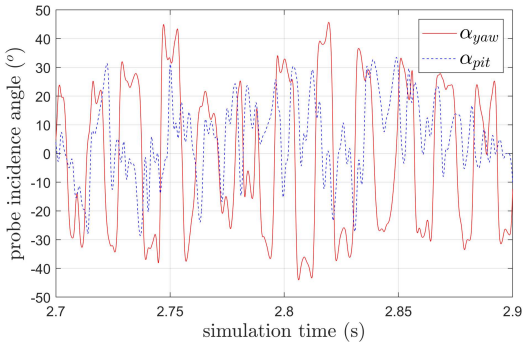

Figure 14: Instantaneous angles at the traverse centreline, URANS (fine mesh).

B. Mesh Sensitivity

Mesh sensitivity was examined by isotropically scaling the freestream cell density while maintaining wall distances. Results at the experimental traverse plane are shown in Figure 15 for a coarse mesh of 2.4 million cells (dashed lines) and the final, finer mesh of 5.8 million cells (solid lines). The drag coefficient for the two meshes, calculated using equation (24), agreed to three significant figures ($C_D = 0.725$).

Figure 15(a) shows the angle fluctuations, including the compound angle which is the most crucial for 5HP errors. The peak value is around 27° at the wake centreline and the two grids agree to within 1° over the entire traverse. Using these values, Figure 15(b) shows predictions of 5HP total pressure error, E_{P0}, from equation (29). The maximum amplitude for the fine grid is $E_{P0} = -0.32$ at the centreline, i.e. 32% of the local dynamic head, and the maximum discrepancy between the two grids is ~0.02.

Figure 15(c) shows total pressure loss coefficient, defined as:

$$Y_P = \frac{P_{01} - P_0}{P_{01} - P_{fs}} \tag{37}$$

where P_{fs} is the static pressure in the freestream outside the wake, $|y/W| > 2$. The time-averaged loss is more diffuse for the coarse grid due to increased numerical dissipation, with a maximum discrepancy of ~0.02 at the centreline. This value is close to the estimated convergence uncertainty. The plot also includes predictions of 5HP-indicated loss using the values of E_{P0} from Figure 15(b). The local dynamic pressure at the wake centreline is $\sim 0.62(P_{01} - P_{fs})$, so $E_{P0} = -0.32$ corresponds to an overestimation of ~0.20 in Y_p. As seen in the plot, the 5HP-indicated loss is up to ~40% higher than the time-mean. Again, the two grids give similar values with a maximum discrepancy of 0.03 at the centreline.

The surface static pressure coefficients for the two meshes are also compared in Figure 11. The coarse mesh gives a lower base pressure (higher C_p) on the trailing face of the body, in part because

it predicts higher wake blockage (i.e. lower freestream pressure) downstream of the body. The fine mesh is in close agreement with the experiments and gives a similar value of form drag (0.80 vs. 0.74).

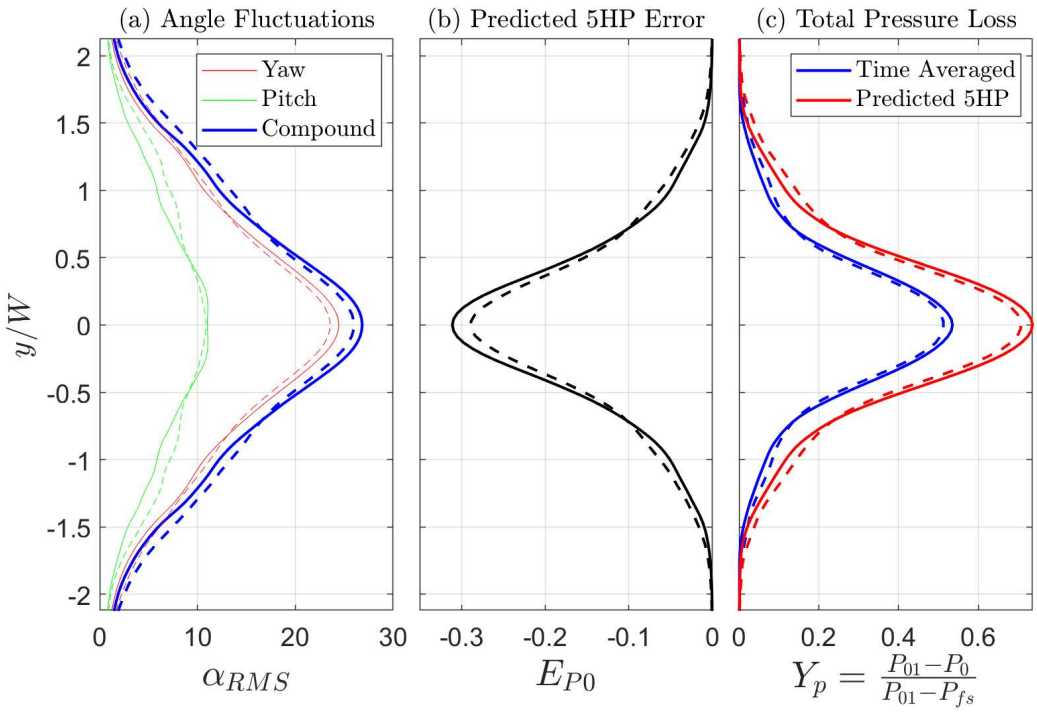

Figure 15: Mesh sensitivity at the wake traverse plane. Solid lines: fine mesh (5.8M cells); dashed lines: coarse mesh (2.4M cells). Prediction of 5HP response using equation (29).

VI. Results and Analysis

This section presents the wake measurements and computations. The 5HP errors are first quantified experimentally by comparison with the Kiel data. Comparison with the CFD then shows that it is vital to mimic the probe response to obtain a true like-for-like comparison with the 5HP data. Finally, we demonstrate how to correct the 5HP data using the URANS flow angles.

A. Experimental Demonstration of 5HP Errors

Figure 16(a) shows traverse measurements of total pressure loss from the 5HP and the Kiel probe. The Kiel is largely insensitive to angle so has minimal fluctuating angle error. The 5HP

indicates losses which are 0.22 (+44%) higher at the wake centreline, and are in line with the predictions shown in Figure 15(c).

Figure 16(b) presents static pressure coefficient, C_{ps}, defined in a similar manner to loss:

$$C_{ps} = \frac{P_{01} - P}{P_{01} - P_{fs}} \tag{38}$$

Compared to the sidewall statics, the 5HP indicates that the pressure at midspan is lower by $\sim 0.30(P_{01} - P_{fs})$. The error in this measurements will become apparent in the following subsection.

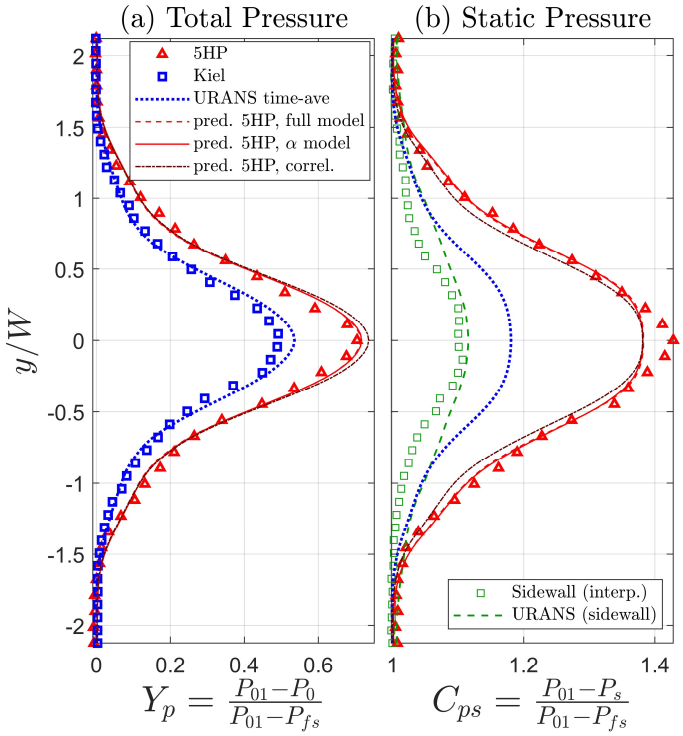

Figure 16: Total and Static Pressure in the wake: experiments and URANS with models of 5HP response.

B. Validating CFD by Mimicking 5HP Probe Response

The time-average of the URANS calculations is included in Figure 16. Total pressure (Figure 16(a)) is close to the Kiel measurements but the wake appears somewhat under-mixed, with higher loss at the centreline. Sidewall static pressure in Figure 16(b) is close to the measurements, especially at the centreline. URANS predicts that the midspan pressure is only $\sim 0.10(P_{01} - P_{fs})$ below the sidewall value, i.e. the pressure is significantly higher than indicated by the 5HP.

To mimic the 5HP response, the time-series of flow angles and pressure from the URANS calculation can be directly inputted into the quasi-steady model outlined in §II. Mimicking the probe response in this way gives a like-for-like comparison between the experiments and CFD. The instantaneous angles exceed the calibration range (±26°) and the map was therefore extended by linearly extrapolating individual hole coefficients (equation (4)). This extrapolation introduces only small uncertainty since similar results were obtained by clipping the flow angles to ±26°. The modelled response of the 5HP is included in Figure 16 using three methods: (1) the "full model", where flow angles, total and static pressure fluctuations are inputted into the quasi-steady model. This case overlays almost exactly with (2) the "α model", where *only flow angles* are input into the quasi-steady model. The final method (3) uses the correlation in equation (30) based on the RMS fluctuating flow angles.

All three models correctly mimic the behaviour of the 5HP, and thus allow a like-for-like comparison of the CFD and 5HP data. The first two models are almost indistinguishable, demonstrating that it is the angle fluctuations that drive the error. The reason is highlighted in Figure 17, which shows that pressure fluctuations are not strongly correlated with the yaw angle fluctuations. Pressure fluctuations are therefore ignored in all following corrections. The correlation in Figure 16 returns similar predictions to the model with the advantage of being much simpler to apply.

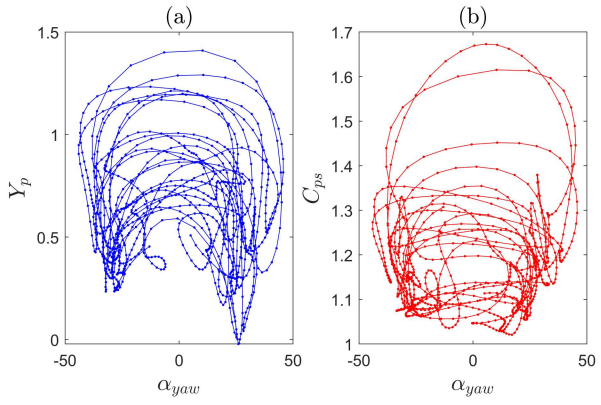

Figure 17: (a) Total and (b) Static pressure correlation with yaw angle, wake centreline.

C. Correcting Experimental Errors using URANS Flow Angles

The quasi-steady model and correlations can also be used to correct pneumatic-averaging errors in experimental data, provided we have an estimate of the unsteady flow angles. In general this could be measured experimentally, but here we use the CFD predictions. As discussed in the following section, this approach has the advantage of being able to be applied more generally – especially for the correction of historical data.

In a similar manner to the previous section, URANS flow angles can be used to correct the 5HP measurements either by (1) direct calculation, inputting the time-series of flow angles into the quasi-steady model with a known calibration map, or (2) applying the correlations given in equations (29)→(31).

Using the direct calculation method, the response model calculates the difference between the true time-averaged coefficients, e.g. $\bar{C}_{P0}$, and those indicated by the probe, e.g. $\hat{C}_{P0}$. Applying these differences to the indicated coefficients allows a direct correction of the data, e.g. for total pressure:

$$C_{P0-cor} = \hat{C}_{P0} + \left[\bar{C}_{P0} - \hat{C}_{P0}\right]_{model} \tag{39}$$

$$\bar{P}_{0-cor} = \bar{P}_c + (\bar{P}_c - \bar{P}_{ave})C_{P0-cor} \tag{40}$$

Figure 18 shows that this correction, labelled "5HP direct calc.", brings the 5HP total pressure in line with the Kiel (dashed blue line), and the static pressure is now in good agreement with URANS. Overall, the errors have been reduced by about an order of magnitude.

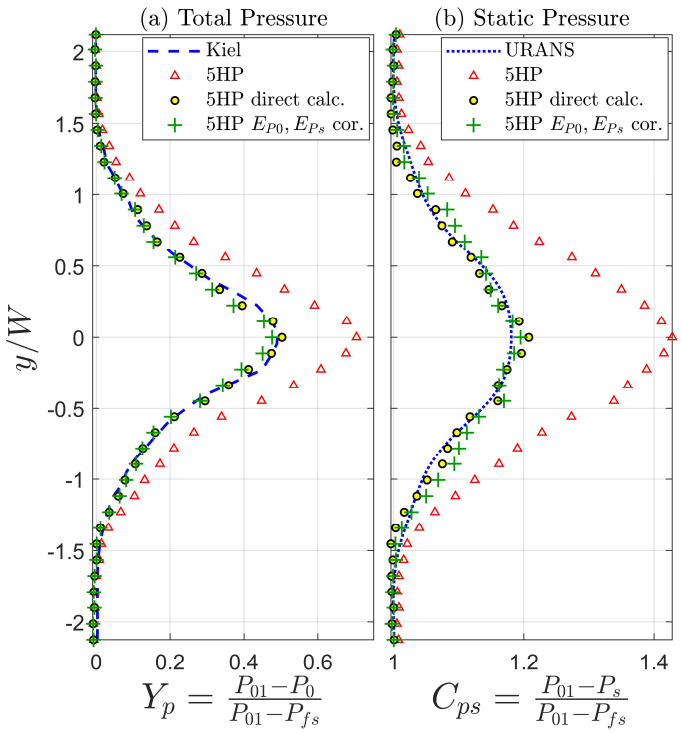

Figure 18: Correction of 5HP data using URANS flow angles: quasi-steady model ("direct calc") and correlations (equations (29), (30)).

The second approach uses the correlations based on the standard deviation of the compound angle. This approach has the advantage of being very simple to apply and does not require the probe calibration map. For this 45° angle 5HP, the total and static errors are of similar magnitude (equation (30)):

$$E_{PS} \approx E_{P0} \approx -1.61 \times 10^{-4} \left(\alpha_{comp-RMS}\right)^{2.3} \tag{41}$$

From equations (23) and (24), the corrected total and static pressure are then given by:

$$\bar{P}_0 = \frac{\hat{P}_0(1 - E_{PS}) + \hat{P}_s E_{P0}}{(1 - E_{PS} + E_{P0})} \tag{42}$$

$$\bar{P}_s = \hat{P}_s(1 + E_{P0}) - \hat{P}_0 E_{PS} \tag{43}$$

As Figure 18 shows, this method gives a similar correction to the direct calculation but is slightly less accurate.

Table 1 compares calculated drag coefficients calculated with equations (34) and (35). The uncorrected 5HP indicates a drag coefficient of 1.18, around 60% higher than the experimental form drag. The direct calculation correction brings the value to within 3% of the calculated form drag, and the correlation correction is within 7%.

			5HP		
	URANS	Surface Statics	Indicated	Direct Correction	E_{P0}, E_{Ps} Correlation
C_{D-form}	0.80	0.74	-	-	-
C_D	0.72	-	1.18	0.72	0.69

Table 1: Calculated Drag Coefficients.

VII. Discussion: General Implications

This section considers the general implications of the results. In the presence of fluctuating flow angles, pneumatic-averaging errors affect a wide variety of pneumatic probes; a significant body of data is therefore likely to be corrupted. We first consider some common set-ups where angle fluctuations may be significant. We then consider the implications for CFD validation, practical steps to post-correct experimental data, and how to minimize angle fluctuation errors in experiments.

A. Common Set-Ups with Significant Flow Angle Fluctuations

We have demonstrated that fluctuating angles can cause large errors in bluff-body shedding wakes. Significant errors may also be expected in any flow where unsteady shear layers generate flow angle fluctuations. Examples include stalled aerofoils or diffusers, trailing edge shedding, and three-dimensional unsteady flows such as tip leakage, corner separation and stall in turbomachinery flows. Similar pneumatic-averaging errors would be expected for any multi-hole probe or unshrouded pitot.

Measurements in turbomachines are particularly prone to pneumatic-averaging errors because of blade-passing fluctuations. Turbine efficiency is typically calculated from shaft torque and

stationary-frame 5HP area-traverses, e.g. [2], [3]. These 5HP measurements will be corrupted by periodic unsteadiness from upstream rotating blade rows. There is direct evidence of such errors in the comparison of Kiel and 5HP data in Bauinger et al. [2]. Coull et al. [16] estimated that angle fluctuations can lead to under-estimation of turbine efficiency by up to 1.5%. Such errors are large enough to warrant the post-correction and reinterpretation of a wide body of data.

B. Implications for CFD Validation

When significant flow unsteadiness is present, Figure 16 demonstrates the need to mimic the probe response to obtain a true like-for-like validation of CFD against experiments. To further illustrate this point, we present a preliminary validation exercise for the T106C linear cascade turbine reported by Michálek et al. [18]. A 5HP was used to traverse the blade wake. At a Reynolds number of 80,000 (based on true chord and exit conditions) and an exit Mach number of 0.65, the blade suction surface has a partially open separation which will lead to the shedding of vortical structures into the wake. As summarised by Cengiz et al. [19], this test case is a challenging test case for the CFD community: multiple authors have used computationally intensive Direct Numerical Simulation (DNS) and Large Eddy Simulation (LES), but the time-average of these simulations consistently under-predicts the experimental total pressure loss.

For the smooth-wall LES simulation of Cengiz et al. [19], data from four numerical probes at the traverse plane are assessed to examine the effect of flow unsteadiness. Figure 19(a) shows that the RMS angle fluctuations are around 12° at the wake centreline. Figure 19(b) shows the total pressure losses: the 5HP data shows significantly higher loss than the time-average from the LES (blue circles). Using equation (29) with the RMS angle fluctuations, the predicted 5HP response (red triangles) is around 0.01 higher than the time-average in the wake. While the mid-wake loss is still underpredicted, modelling the probe response in this way significantly improves the agreement between CFD and experiments.

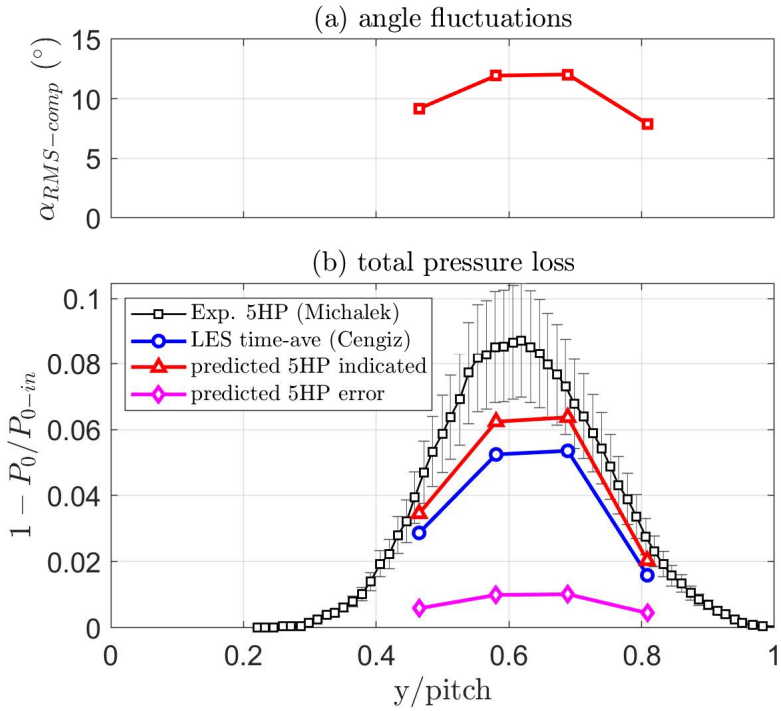

Figure 19: Accounting for Flow Unsteadiness in the comparison of experiments and CFD for the T106C turbine blade, [18], [19].

C. Assessing and Correcting Experimental Errors

We can assess pneumatic-averaging errors provided we have an estimate of probe incidence fluctuations. This information may be obtained from measurements (e.g. multi-element hot-wires), or from an analytical/computational prediction (as in the current example). As illustrated above, the correlations and/or quasi-steady model can then be used to correct errors in the experimental data.

It is notable that we have not found any direct means of identifying problems with 5HP data, such as the error-detection methods proposed by Yasa and Paniagua [17] and Grimshaw and Taylor [1]. These detection methods examine the departure of measured data from the individual hole calibration maps, which is observed in shear layers and in proximity to walls. However, this type of approach is not reliable for angle fluctuations because some erroneous measurements still lie close to the calibration maps.

D. Designing-Out Experimental Error

Finally, it is useful to consider how we can design experiments to minimise the errors from angle fluctuations. Several key observations can be made:

- Kiel probes should be used to cross-check 5HP data when fluctuations may be present.
- Turbomachinery traverses downstream of rotors should be performed in the rotating frame where possible to minimise fluctuations. Alternatively, stationary-frame traverses should be performed as far downstream as possible to allow more mixing to take place.
- Errors can be avoided by use of fast-response multi-hole probes. More work is needed to further miniaturise such probes to improve their spatial accuracy, which is not yet acceptable for many applications.
- Errors could be minimised with new multi-hole probes with low angle sensitivity for total and static pressure. For example, a hybrid 5HP with a Kiel-pitot central hole would be much less prone to errors. Challenges remain to develop, characterise and miniaturise such designs.

VIII. Conclusions

Quasi-steady arguments demonstrate how fluctuating incidence leads to pneumatic-averaging errors. Five-hole-probe calibration coefficients for total and static pressure have an approximately symmetric response to incidence angle, i.e. the probe has a similar response to both positive and negative incidence. When probe incidence fluctuates, the time-average therefore contains a bias, which cannot be accounted for by the steady calibration. Other multi-hole pneumatic probes and un-Kieled pitots will suffer similar errors.

The errors caused by fluctuating flow angles have been demonstrated in a shedding bluff-body wake. Compared to a Kiel probe, a five-hole-probe over-estimates total pressure loss by up to 44% and under-estimates static pressure, leading to a ~60% over-estimation of drag coefficient. These effects can be accurately predicted using a URANS calculation together with the quasi-steady model

of probe response. This modelling of the probe pneumatic-averaging is necessary to obtain a true like-for-like validation of CFD against experiments.

Post-correction of experimental data can be achieved if the unsteady flow angles are measured or simulated. Using the URANS predictions, a simple correction is made using correlations based on the standard deviation of the compound angle. A more accurate correction uses the probe calibration map and flow time-series to predict the quasi-steady response. Both methods reduce errors by around an order-of-magnitude.

A wide body of published and industrial data is likely to have been corrupted by fluctuating angle errors, in particular turbomachinery performance measurements. The approaches given in the paper can be used to analyse the likely errors and post-correct this data. Experiments should be planned to mitigate these errors, for example by corroborating multi-hole probe data with Kiel probes.

Funding Sources

The authors would like to thank Rolls-Royce plc. for funding this work.

Acknowledgements

The authors would like to thank Rolls-Royce for funding and permission to publish, with particular thanks to Dr Raul Vazquez and Dr Duncan Simpson. Prof Luca di Mare, University of Oxford, provided advice on the URANS calculation set-up. Dr Sam Grimshaw of the Whittle Laboratory, University of Cambridge, provided a sample calibration map.

References

[1] Grimshaw, S.D. and Taylor, J.V., 2016. "Fast settling millimetre-scale five-hole probes." *ASME Turbo Expo: Power for Land, Sea, and Air, June 2016*

DOI: http://dx.doi.org/10.1115/GT2016-56628

[2] Bauinger, S., Marn, A., Göttlich, E. and Heitmeir, F., 2017, "Influence of pressure fluctuations on the mean value of different pneumatic probes." *International Journal of Turbomachinery, Propulsion and Power,* 2(3), p.13.

DOI: http://dx.doi.org/10.3390/ijtpp2030013

[3] Evans, K.R. and Longley, J.P., 2017. “Clocking in low-pressure turbines.” *Journal of Turbomachinery*, 139(10), p.101003.

DOI: http://dx.doi.org/10.1115/1.4036341

[4] Prahst, P.S., Kulkarni, S. and Sohn, K.H., 2015. “Experimental results of the first two stages of an advanced transonic core compressor under isolated and multi-stage conditions.” *ASME Turbo Expo: Power for Land, Sea, and Air,* June 2015

DOI: http://dx.doi.org/10.1115/GT2015-42727

[5] Melzer, A.P. and Pullan, G., 2019. “The role of vortex shedding in the trailing edge loss of transonic turbine blades.” *Journal of Turbomachinery*, 141(4), p.041001.

DOI: http://dx.doi.org/10.1115/1.4041307

[6] Goldstein, S., 1936. “A note on the measurement of total head and static pressure in a turbulent stream.” *Proceedings of the Royal Society of London. Series A-Mathematical and Physical Sciences,* 155(886), pp.570-575.

[7] Bailey, S.C.C., Hultmark, M., Monty, J.P., Alfredsson, P.H., Chong, M.S., Duncan, R.D., Fransson, J.H.M., Hutchins, N., Marusic, I., McKeon, B.J., Nagib, H.M., Örlü, R., Segalini, A., Smits, A.J., and Vinuesa, R., 2013, “Obtaining Accurate Mean Velocity Measurements in High Reynolds Number Turbulent Boundary Layers Using Pitot Tubes,” *J. Fluid Mech.,* 715, pp. 642–670

DOI: https://doi.org/10.1017/jfm.2012.538

[8] Bradshaw, P. & Goodman, D.G., 1968, “The effect of turbulence on static-pressure tubes.” *Reports and Memoranda 3527, Aeronautical Research Council.*

[9] Christiansen, T. & Bradshaw, P., 1981, “Effect of turbulence on pressure probes.” *Journal of Physics E: Scientific Instruments* 14 (8), 992–997

DOI: http://dx.doi.org/10.1088/0022-3735/14/8/024

[10] Dominy, R.G. and Hodson, H.P., 1993, “An investigation of factors influencing the calibration of five-hole probes for three-dimensional flow measurements.” *Journal of Turbomachinery*, 115(3), pp.513-519.

DOI: http://dx.doi.org/10.1115/1.2929281

[11] Grimshaw, S.D., 2020, private communication

[12] Ng, H.C.H. and Coull, J.D., 2017. “Parasitic loss due to leading edge instrumentation on a low-pressure turbine blade.” *Journal of Turbomachinery*, 139(4).

DOI: http://dx.doi.org/10.1115/1.4035043

[13] Jones, B.M., 1936. “Measurement of profile drag by the pitot-traverse method.” Reports and Memoranda 1688, Aeronautical Research Council.

[14] ANSYS Fluent Theory Guide, Release 18.0., 2017. *ANSYS Inc.: Canonsburg, PA, USA*.

[15] Menter, F.R. and Egorov, Y., 2010. “The scale-adaptive simulation method for unsteady turbulent flow predictions. Part 1: theory and model description.” *Flow, Turbulence and Combustion*, 85(1), pp.113-138.

DOI: http://dx.doi.org/10.1007/s10494-010-9264-5

[16] Coull, J., Dickens, T., Ng, H. and Serna, J., 2020, “Five hole probe errors caused by fluctuating incidence.” *XXV Symposium on Measuring Techniques in Turbomachinery, Santorini, Greece, Sept 2020*

DOI: *http://dx.doi.org/10.1051/e3sconf/202234501006*

[17] Yasa, T. and Paniagua, G., 2012. “Robust procedure for multi-hole probe data processing.” *Flow Measurement and Instrumentation*, 26, pp.46-54.

DOI: http://dx.doi.org/10.1016/j.flowmeasinst.2012.03.004

[18] Michálek, J., Monaldi, M. and Arts, T., 2012. Aerodynamic performance of a very high lift low pressure turbine airfoil (T106C) at low Reynolds and high Mach number with effect of free stream turbulence intensity. Journal of Turbomachinery, 134(6).

DOI: https://doi.org/10.1115/1.4006291

[19] Cengiz, K., Kurth, S., Wein, L. and Seume, J.R., 2022, “Implicit Large-Eddy Simulation of a Rough Turbine Blade Using High-Order Curved Elements.” Proceedings of Global Power and Propulsion Society, GPPS Chania22 18th-20th September 2022

DOI: 10.33737/gpps22-tc-21